Diagnostic of the spectral properties of Aquila X-1 by Insight-HXMT snapshots during the early propeller phase

C. Güngör [a,b,*], M.Y. Ge [a], S. Zhang [a], A. Santangelo [a,c], S.N. Zhang [a,d,e], F.J. Lu [a], Y. Zhang [a,d], Y.P. Chen [a], L. Tao [a], Y.J. Yang [a], Q.C. Bu [a], C. Cai [a,d], X.L. Cao [a], Z. Chang [a], G. Chen [a], L. Chen [f], T.X. Chen [a], Y. Chen [a], Y.B. Chen [g], W. Cui [a,g], W.W. Cui [a], J.K. Deng [g], Y.W. Dong [a], Y.Y. Du [a], M.X. Fu [g], G.H. Gao [a,d], H. Gao [a,d], M. Gao [a], Y.D. Gu [a], J. Guan [a], C.C. Guo [a,d], D.W. Han [a], Y. Huang [a], J. Huo [a], L. Ji [b], S.M. Jia [a], L.H. Jiang [a], W.C. Jiang [a], J. Jin [a], L.D. Kong [a,d], B. Li [a], C.K. Li [a], G. Li [a], M.S. Li [a], T.P. Li [a,d,g], W. Li [a], X. Li [a], X.B. Li [a], X.F. Li [a], Y.G. Li [a], Z.W. Li [a], X.H. Liang [a], J.Y. Liao [a], C.Z. Liu [a], G.Q. Liu [g], H.W. Liu [a], X.J. Liu [a], Y.N. Liu [g], B. Lu [a], X.F. Lu [a], T. Luo [a], Q. Luo [a,d], X. Ma [a], B. Meng [a], Y. Nang [a,d], J.Y. Nie [a], G. Ou [a], N. Sai [a,d], L.M. Song [a], X.Y. Song [a], L. Sun [a], Y. Tan [a], Y.L. Tuo [a,d], C. Wang [d,e], G.F. Wang [a], J. Wang [a], W.S. Wang [a], Y.S. Wang [a], X.Y. Wen [a], B.B. Wu [a], B.Y. Wu [a,d], M. Wu [a], G.C. Xiao [a,d], S. Xiao [a,d], S.L. Xiong [a], Y.P. Xu [a], J.W. Yang [a], S. Yang [a], Y.J. Yang [a], Q.B. Yi [a,d], Q.Q. Yin [a], Y. You [a,d], A.M. Zhang [a], C.M. Zhang [a], F. Zhang [a], H.M. Zhang [a], J. Zhang [a], T. Zhang [a], W. Zhang [a,d], W.C. Zhang [a], W.Z. Zhang [f], Y. Zhang [a], Y.F. Zhang [a], Y.J. Zhang [a], Z. Zhang [g], Z.L. Zhang [a], H.S. Zhao [a], X.F. Zhao [a,d], S.J. Zheng [a], D.K. Zhou [b], J.F. Zhou [b], Y. Zhu [a], Y.X. Zhu [a]

[a] *Key Laboratory of Particle Astrophysics, Institute of High Energy Physics, Chinese Academy of Sciences, 19B Yuquan Road, Shijingshan District, 100049, Beijing, China*
[b] *Istanbul University, Science Faculty, Department of Astronomy and Space Sciences, Beyazit, 34119, Istanbul, Turkey*
[c] *Institut für Astronomie und Astrophysik, Universität Tübingen, Sand 1, D 72076 Tübingen, Germany*
[d] *University of the Chinese Academy of Sciences, 100049, Beijing, China*
[e] *National Astronomical Observatories, Chinese Academy of Sciences, Beijing 100012, China*
[f] *Department of Astronomy, Beijing Normal University, Beijing 100088, China*
[g] *Department of Physics, Tsinghua University, Beijing 100084, China*

ARTICLE INFO

ABSTRACT

We study the 2018 outburst of Aql X-1 via the monitor of all sky X-ray image (MAXI) data. We show that the outburst starting in February 2018 is a member of *short-low* class in the frame of outburst duration and the peak count rate although the outburst morphology is slightly different from the other fast-rise-exponential-decay (FRED) type outbursts with a milder rising stage. We study the partial accretion in the weak propeller stage of Aql X-1 via the MAXI data of the 2018 outburst. We report on the spectral analysis of 3 observations of Aquila X-1 obtained by Insight – hard X-ray modulation telescope (Insight-HXMT) during the late decay stage of the 2018 outburst. We discuss that the data taken by Insight-HXMT is just after the transition to the weak propeller stage. Our analysis shows the necessity of a comptonization component to take into account the existence of an electron cloud resulting photons partly up-scattered.

1. Introduction

Low mass X-ray binaries (LMXBs) are systems containing a black hole (BH) or a neutron star (NS) and a low mass companion ($M_c \lesssim 1 \, M_\odot$). The mass accretion mechanism in these systems is Roche lobe overflow (Frank et al., 2002). The low mass com-

panion fills its Roche lobe during its evolution and the material is being transferred from the first Lagrange point to the Roche lobe of the compact object. Since the transferring material has angular momentum, it creates an accretion disk around the compact object instead of falling onto its surface directly (Pringle and Rees, 1972). LMXBs may possible be incubators of millisecond pulsars. Accretion onto NS can be the reason of conversion from the slow rotating NS with high magnetic field to the fast spinning and low magnetic field NS, so called recycling scenario (Bhattacharya and van den Heuvel, 1991; Tauris and van den Heuvel, 2006).

In the case of that the compact object is a NS, the disk material interacts with the magnetic field –the disk magnetosphere interaction. The disk magnetosphere interaction shows different stages according to the location of the inner radius of disk:

(i) *The accretion stage*: If the inner radius of the disk is closer to the NS than the corotation radius,[1] all of the material reaching to the inner layers is being transferred onto the NS.
(ii) *The propeller stage*: The inner radius of the disk is located within-inside the light cylinder[2] and close to the corotation radius (Illarionov and Sunyaev, 1975), the material reaching to inner layers is dispersed for an ideal thin disk (full propeller). If the inner layers of the disk have a scale height then a fraction of the material can reach onto the poles (weak propeller, Ekşi and Kutlu, 2011) until the inner layers shrink back and the system becomes full propeller.
(iii) *The radio pulsar stage*: If the inner radius of the disk is located out of the light cylinder, the system acts as an isolated neutron star with no accretion.

A LMXB completes these disk magnetosphere interaction stages along its billion years evolution. Accreting millisecond X-ray pulsars (AMXPs) constitute a subset of LMXBs in which X-ray pulsations are detected, and they are peerless sources to study the evolution of LMXBs since they show disk magnetosphere interaction stages in an observable duration.

Aql X-1 is an NS-LMXB accompanying a $K4 \pm 2$ main sequence star, rotating with the period of 19 h in a $36° - 47°$ inclined orbit (Mata Sánchez et al., 2017). Aql X-1 is also classified as an AMXP (Koyama et al., 1981) with its intermittent pulsations with the pulse frequency of 550.27 Hertz detected only for 150 s overall 23 years of observations (Casella et al., 2008) in which the detected pulse frequency is consistent with the burst oscillations (Casella et al., 2008). Aql X-1 is classified as soft X-ray transient (SXT) showing cyclic outburst almost each year in its X-ray light curve. The X-ray Luminosity of the source in the quiescent state is $L_X \approx 10^{33}$ erg s^{-1} (Verbunt et al., 1994) while the outburst peak luminosity can exceed $L_X \approx 10^{37}$ erg s^{-1} (Campana et al., 2013). Jonker and Nelemans (2004) reported the distance of the source as $4.4 - 5.9$ kpc using the burst peak flux from the Rossi X-ray timing explorer (RXTE) data.

Although Aql X-1 is one of the most studied source, studies on this source may still shed light on a lot of open problems such as the physical origin of the intermittency of the pulsations. The effect of comptonization to smear out pulsations has been argued in Göğüş et al. (2007) who has not found any confirmation of such mechanism in three sources (GX 9+1, GX 9+9 and Sco X-1). As they mentioned the sample set must be enlarged to generalize the outcome. The observations, not only in outburst but also in quiescent state, may allow us to study the time evolution of the crust temperature and model crust cooling scenario. In Aql X-1 case, the
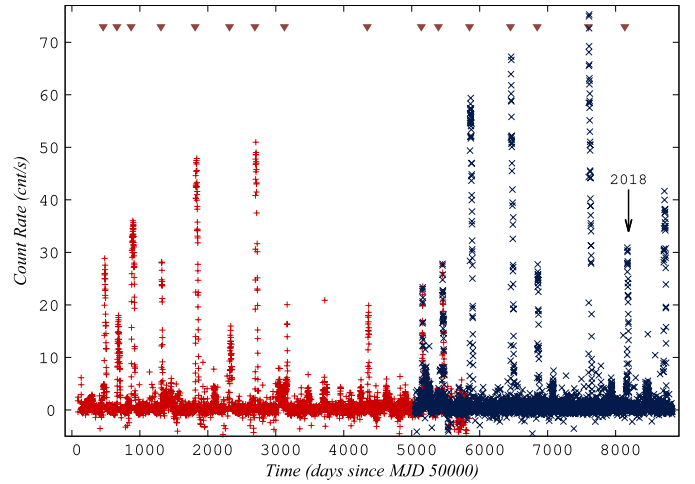

Fig. 1. The long term light curve of Aql X-1 since 1996, using the data from the ASM (dark red pluses) and the MAXI (dark blue crosses). The count rates are given in the ASM level in which the MAXI count rates are calibrated as explained in section 2. The brown upside-down triangles show the FRED type outbursts and the black arrow indicates the 2018 outburst whose decay stage has been partly observed by Insight-HXMT. (For interpretation of the colours in the figure(s), the reader is referred to the web version of this article.)

outbursts are very frequent and there is no enough time between two outbursts to reach crust−core equilibrium (Ootes et al., 2018). Spectral and temporal studies with Insight-HXMT data may play key role to address these open questions on LMXBs as well as the other X-ray space missions.

In this work, we present the spectral analysis outcome of the Insight-HXMT data. We explain the details of the data reduction and present our results of the spectral analysis in section 2. In section 3, we discuss the 2018 outburst in the frame of outburst classification suggested by Güngör et al. (2014) and the partial accretion in the propeller stage (Güngör et al., 2017b). We also present the discussion on the spectral outcome of Insight-HXMT data in section 3. Finally, we conclude our study in section 4.

2. Observation and data analysis

We show the 23 year light curve of Aql X-1 in Fig. 1 using the data taken by All-Sky Monitor (ASM; Lochner and Remillard, 1995)[3] mounted on RXTE and the MAXI[4] (Matsuoka et al., 2009) mounted on the international space station (ISS). The MAXI count rates are multiplied by 21.5 to calibrate to the ASM level by using the peak count rates of the 2009 and the 2010 outbursts which were jointly observed. We used the one day binned MAXI data in the energy range of $2.0 - 20.0$ keV to study the outburst starting in February 2018. We obtained the hardness values during the 2018 outburst using the ratio of the MAXI count rates in $2.0 - 10.0$ keV to the ones in $10.0 - 20.0$ keV. The MAXI light curve and the hardness evolution are used to classify the 2018 outburst and to obtain the fastness parameters[5] for a given time using the method presented in section 3.

Insight-HXMT (Li, 2007; Zhang et al., 2014) is the first Chinese X-ray space mission launched on 15th of June 2017. It has three main detectors sensitive to different energy ranges: (i) The low-energy detector (hereafter *LE*) operates the Swept Charge Device sensitive to the energy range of $1.0 - 15.0$ keV whose effective area is 384 cm^2. LE has two different field of view (FoV) options;

---

[1] The radius that the angular velocity of the star is equal to the Keplerian angular velocity.

[2] The cylinder centred on the pulsar and aligned with the rotation axis at whose radius, the corotating speed equals the speed of light.

[5] A ratio of the angular velocity of the star to the Keplerian angular velocity at the inner disk radius $\omega_* \equiv \Omega_*/\Omega_K(R_{in})$.

Table 1

Some properties of the Insight-HXMT observations and the best fit parameters of *blackbody + power law* model (*model I*), *blackbody + disk blackbody* model (*model II*), *blackbody + comptonization* model (*model III*), *disk blackbody + comptonization* model (*model IV*), and *blackbody + disk blackbody + comptonization* model (*model V*).

ObsID		P011466801001	P011466801002	P011466801003
Date (UTC)		2018/3/19 19:09:24	2018/3/20 19:01:00	2018/3/22 06:00:39
Date (MJD)		58196.798937	58197.793104	58199.251194
Observation mode		Pointing	Pointing	Pointing
Exposure time (ks)		10	10	10
Total count[a]	LE	29371463	38538779	41110899
	ME	116103644	115698283	159916052
Effective count[b]	LE	243040	214303	120770
	ME	3654838	3706650	2357891
ω_*[c]		1.06	1.07	1.09
Model I	kT_{bbody} (keV)	4.64 ± 0.50	8.36 ± 1.76	11.91 ± 4.50
bb+po	Γ	2.58 ± 0.11	2.51 ± 0.10	2.65 ± 0.21
	Hardness[d]	0.143 ± 0.014	0.140 ± 0.021	0.126 ± 0.037
	$\chi^2/d.o.f.$	783/924	824/924	748/835
Model II	kT_{bbody} (keV)	3.62 ± 0.24	5.13 ± 0.59	6.33 ± 1.45
bb+diskbb	kT_{diskbb} (keV)	0.87 ± 0.04	1.00 ± 0.05	1.03 ± 0.12
	Hardness[d]	0.180 ± 0.017	0.183 ± 0.032	0.122 ± 0.094
	$\chi^2/d.o.f.$	854/924	831/924	740/835
Model III	kT_{bbody} (keV)	0.37 ± 0.04	0.55 ± 0.03	0.69 ± 0.07
bb+compTT($T_{Wien} = kT_{bb}$)	τ	2.63 ± 0.33	4.99 ± 0.87	6.94 ± 2.08
	Hardness[d]	0.255 ± 0.013	0.185 ± 0.021	0.103 ± 0.013
	$\chi^2/d.o.f.$	781/924	852/924	732/835
Model IV	kT_{diskbb} (keV)	0.46 ± 0.06	0.78 ± 0.07	0.98 ± 0.11
diskbb+compTT($T_{Wien} = kT_{diskbb}$)	τ	2.74 ± 0.40	5.38 ± 0.94	7.64 ± 2.70
	Hardness[d]	0.127 ± 0.013	0.148 ± 0.022	0.080 ± 0.042
	$\chi^2/d.o.f.$	780/924	835/924	730/835
Model V	kT_{bbody}	0.97 ± 0.06	0.74 ± 0.05	0.76 ± 0.08
bb+diskbb+compTT($T_{Wien} = kT_{bb}$)	kT_{diskbb}	0.48 ± 0.01	0.29 ± 0.01	0.38 ± 0.04
	τ	3.52 ± 0.20	5.66 ± 0.54	7.35 ± 1.69
	Flux[d] (10^{-9} erg/cm^2/s)	0.413 ± 0.009	0.263 ± 0.005	0.077 ± 0.005
	Hardness[e]	0.119 ± 0.011	0.138 ± 0.009	0.074 ± 0.019
	$\chi^2/d.o.f.$	770/922	815/922	727/833

[a] The count rates are the full counts obtained from the detector itself before background subtraction and good time interval corrections.

[b] The effective count rates are the total counts after good time interval corrections before background subtraction.

[c] The values of the fastness parameter are calculated using the L_c obtained from the application of the method and using Equation (4) explained in subsection 3.2.

[d] Flux values are unabsorbed and calculated in the energy range of 2–20 keV using *cflux* task in xspec.

[e] Hardness parameters are obtained using the unabsorbed flux ratio of two different energy ranges; $F(10.0 - 20.0 \text{ keV})/F(2.0 - 10.0 \text{ keV})$.

the small FoV, $1.6° \times 6°$, and the big FoV, $6° \times 6°$. There are also three full blocked detectors (also called blind detectors) on LE to estimate the internal gain and the background contribution. *(ii)* The medium-energy detector (hereafter *ME*) consist of 1728 Si-PIN detectors sensitive to $5.0 - 30.0$ keV energy band with the total effective area of 952 cm^2. The FoV options of ME are the Small FoV of $1° \times 4°$, and the big FoV of $4° \times 4°$. There are also three groups of blind detectors in which each group has 32 Si-PIN blind detectors to calculate the background components. *(iii)* The high-energy detector (hereafter *HE*) made by 18 cylindrical NaI(Tl)/CsI(Na) PHOSWICH detectors sensitive to $20.0 - 250.0$ keV with an additional blind detector. The FoV options for HE are $5.7° \times 1.1°$ and $5.7° \times 5.7°$. The large total effective area of 5100 cm^2 in the hard X-ray band is the main advantage of Insight-HXMT.

Aql X-1 is included in the observation list of Insight-HXMT as time of opportunity (ToO) source. Unfortunately, when Aql X-1 underwent to the 2018 outburst, the source was unobservable by Insight-HXMT because of the criteria on the solar avoidance angle which must be greater than 70°. Aql X-1 has been observed by Insight-HXMT three times in March 2018 when the solar avoidance criteria has been passed and the source was still bright enough. Although the observations do not cover whole outburst, they are still valuable to study the spectral properties during the transitions to quiescent state. The LE, the ME and the HE detectors were

active simultaneously during observations and the exposure time was 10 ks for each pointing. The total count rates before and after the good time interval corrections are listed in Table 1 for each detector and each data set. The data from the HE detector are not considered in the analysis because the source is background-dominated.

The data analysis has been done using the latest version of Insight-HXMT data analysis software (HXMTDAS) v2.0.[6] We limited the pointing offset angle to 0.1° to avoid the slew data. We constrained the maximum elevation angle of 12° for LE and 10° for ME. Additionally for the LE detector, we bounded the elevation angle of bright earth as 40°. We set the maximum of geomagnetic cut-off rigidity to 8 GV for both LE and ME. After we filtered the data using the criteria above, we obtained the spectra and the light curves by choosing the small FoV for each detector ($1.6° \times 6°$ for LE and $1° \times 4°$ for ME). We also used the blind detectors to estimate the background spectra and light curves. Using the blind detectors to estimate background level has been tested with the blank sky observations by Insight-HXMT calibration team for the feasibility of this method. We created the response matrix files using the *lerspgen* and *merspgen* tasks in HXMTDAS for transforming the channel number to energy.
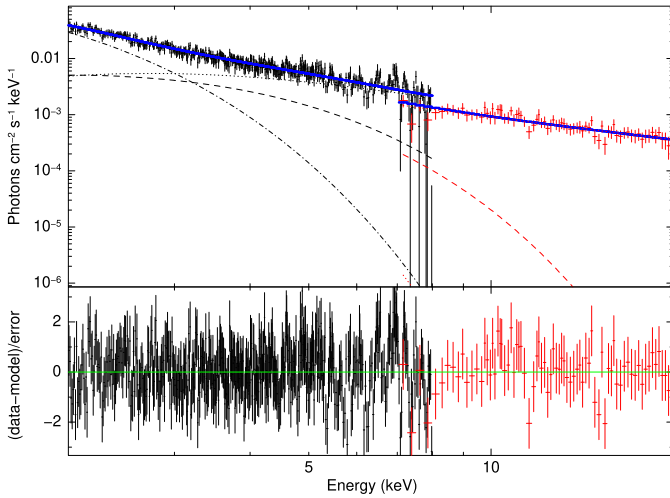
---

[6] http://www.hxmt.org/index.php/dataan/.

Fig. 2. An example spectrum of Insight-HXMT observations of Aql X-1 in the energy range of $2.0 - 20.0$ keV, combination of LE (black) and ME (red) detectors (ObsID O011466801001). The best fits of the *bb+diskbb+compTT* model (*V*) are shown with blue line. Lower panel presents the residuals in terms of sigma.

We modelled the spectra by using the 12.10.0c version of XSPEC package[7] (Arnaud, 1996). We obtained spectra using each channel without grouping. We used the energy range of $2.0 - 8.0$ keV and $7.0 - 20.0$ keV for the LE and the ME detectors, respectively. We added 1.0% systematic error to take into account instrumental uncertainties (Chen et al., 2019). We applied *phabs* as a photoelectric absorption model with the default cross-section in XSPEC version 12.0 (Verner et al., 1996). The neutral hydrogen column density is fixed to $N_H = 3.4 \times 10^{21}$ cm^{-2} (Maccarone and Coppi, 2003). After we loaded the LE data as group 1 and the ME data as group 2, we multiplied the whole model with a constant value to calibrate the normalization levels of the detectors. We fixed this constant to 1.0 for LE and the one for ME kept as the free parameter of the fit while all other free model parameters are linked among LE and ME spectra. We applied a set of models to represent the spectra; blackbody + power law (model I), blackbody + disk blackbody (model II), blackbody + comptonization (model III), disk blackbody + comptonization (model IV) and blackbody + disk blackbody + comptonization (model V). We used *compTT* in XSPEC as the comptonization model (Titarchuk and Lyubarskij, 1995). The plasma temperature of *compTT* is fixed to 15.0 keV (Göğüş et al., 2007) while the input soft photon (Wien) temperature is linked to the temperatures of the blackbody components in model III and V assuming that the source of the up-scattered photons is the NS poles, and to the disk blackbody temperature in model IV. In order to take into account the effectiveness of the iron line, we checked the quality of the models adding a Gaussian component with fixed central line energy of 6.4 keV and the line width of 0.6 keV to each model. Differently from RXTE data (Güngör et al., 2014, 2017b), Gaussian component was not statistically necessary. We also obtained the hardness values for each data set using the ratio of the unabsorbed flux in the energy range of $2.0 - 10.0$ keV to the ones in the energy range of $10.0 - 20.0$ keV using the cflux task in XSPEC. This energy ranges were chosen to be consistent with the hardness values obtained from MAXI count rates. We present an example spectrum of Insight-HXMT (ObsID: O011466801001) and the best fit of the model V in Fig. 2. We list the output of our analysis in Table 1. A detailed discussion about the physical interpretations of the adopted models is given in subsection 3.3. Hereby, we must mention that the hard X-ray luminosity of Aql

---

X-1 during Insight-HXMT observation is too low and background dominates. So, we could not use the data from the HE detector.

3. Discussion

In order to better interpret the spectral output of Aql X-1 from Insight-HXMT during the decay stage, we first studied the 2018 outburst according to the outburst morphology and the light curve properties.

3.1. Classification of outbursts

FRED and low-intensity-state (LIS) type of outbursts of Aql X-1 were first defined by Maitra and Bailyn (2008) based on the light curve morphology. FRED type outbursts have steep rising and exponential decay while LIS outbursts are the periods when the source is slightly more luminous than the quiescent state level ($\sim 5-10$ cnt/s in ASM; ~ 100 mCrab) with very high optical to soft X-ray flux ratio (Maitra and Bailyn, 2008). Aql X-1 showed a FRED type outburst in February 2018, almost 190 days after the end of a LIS type event started in May 2017. This FRED type outburst reached its maximum on 26th of February 2018 in its X-ray light curve ($2.0 - 20.0$ keV). Spiridonova et al. (2018) reported the peak of Aql X-1 in R band on 1st of March 2018 which is 3 days after its X-ray peak.

Asai et al. (2012) reported different classification depending on the pattern of the relative intensity evolution in the two energy bands below/above 15 keV; slow-type (S-type) and fast-type (F-type) outburst. The S-type outbursts have relatively longer ($\gtrsim 9$ days) initial hard-state, while the F-type outbursts have shorter one ($\lesssim 5$ days). The intensity in the energy range of $15.0 - 50.0$ keV of the S-type outbursts reaches to its maximum in the initial hard-state period and decreases dramatically at the hard-to-soft transition. Differently, the intensity of the F-type of outbursts in the energy range of both $2.0 - 15.0$ keV and $15.0 - 50.0$ keV peaks after the transition. Accordingly, the 2018 FRED type of outburst can be classified as S-type with its $\sim$10 days initial hard-state duration (see bottom panel of Fig. 3).

Another type of classification was presented by Güngör et al. (2014), based on the peak count rate and the duration of the FRED type outbursts. This work excluded the LIS type outbursts since they do not have a systematic outburst pattern. In this study, three outburst types –long-high, medium-low and short-low– were defined and the main physical mechanism to discriminate outburst types is mentioned as the irradiation. Following their methodology, we first smoothed the $2.0 - 20.0$ keV MAXI light curve of the 2018 outburst with Bézier spline method and we re-scaled the times to the outburst onsets. We, then, compared it with all of the other outbursts that Aql X-1 showed (Fig. 4). Hereunder, the 2018 outburst is classified as short-low type with the peak count rate of $\sim$30 cnts^{-1} and the outburst duration of $\sim$30 days, although its rising stage is slightly milder than the other short-low type outbursts.

3.2. Partial accretion in the propeller stage

The decay stages of the light curves of the FRED type outbursts in LMXB systems generally have two different decay trends –the slow and the fast decay stages. The critical *cut-off* point, also called *knee*, between these two stages is mentioned as the possible transition from the accretion stage to the weak propeller stage (Zhang et al., 1998; Gilfanov et al., 1998; Campana et al., 1998; Ibragimov and Poutanen, 2009; Asai et al., 2013). Herein, we have to mention that these *cut-off* behaviours have been observed from the light curves of both NS-LMXBs and BH-LMXBs in which the propeller effect is not expected from the systems with BHs since

they do not have magnetic fields. This cut-off in LMXBs can also be explained via the thermal disk instability model (Lasota, 2001) which is the only scenario for BH-LMXBs while for NS-LMXBs the transition from accretion to propeller stage is an alternative. If the reason of the existence of the knee at the decay stage of Aql X-1 is the same as in BH systems, the technique of calculating the mass fraction rate in the weak propeller stage using the knee would be invalid.

A unique technique, using the X-ray light curve, has been proposed by Güngör et al. (2017b) to calculate the mass accretion rate in the propeller stage as a function of the fastness parameter. The origin of the X-ray luminosity, is the gravitational potential energy of the transferring material,

$$L_X = \frac{GM_* \dot{M}_*}{R_*}, \tag{1}$$

where G is the gravitational constant, M_* and R_* are the mass and the radius of the NS, and $\dot{M}_*$ is the mass accretion rate falling onto the poles of NS. Accordingly, the X-ray luminosity is directly proportional to the mass accretion rate ($L_X \propto \dot{M}_*$). Assuming that the slow decay corresponds to the accretion stage, all of the material reaching the inner layers of the disk ($\dot{M}$) is accreted, therefore, the exponential trend of the slow decay stage gives the time variation of $\dot{M}$. The slow decay can be represented by using the function (Güngör et al., 2017b);

$$L(t) = L_0 \left(1 + \frac{t - t_0}{t_\nu}\right)^{-\alpha}, \tag{2}$$

where t_0 is the time of the peak, L_0 is the luminosity at the time of t_0, and t_ν is the free fit parameter proportional to the timescale of the outburst. α is the power−low index related to the pressure and the opacity in the disk. We used α of 1.25 for the fit in which this value is suitable for a gas pressure dominated disk with bound free opacity (Cannizzo et al., 1990; Ekşi and Kutlu, 2011). This formula also gives $\dot{M}(t)$ from Equation (1). It is assumed that the time variation of $\dot{M}$ follows the same trend in the weak propeller stage in a condition of that time variation of the mass transfer rate throughout the disk continues with the same trend. Thus, the mass transfer ratio of the falling material onto the NS and the material reaching to the inner layers, $f \equiv \dot{M}_*/\dot{M}$, can be obtained via the ratio of the observed luminosity in the fast decay stage and the calculated luminosity from the Equation (2) for the corresponding time. f function is expected to be a step function in the simplest picture of an ideal propeller surrounded by an infinitely thin disk. If the disk has a scale height, the accretion can proceed from higher latitudes of the disk (Romanova et al., 2004; Ekşi and Kutlu, 2011), then, one can expect f as a smoothed step function;

$$f = \frac{1}{2}\left[1 + f_{\min} + (1 - f_{\min})\tanh\left(\frac{\omega_c - \omega_*}{\delta}\right)\right], \tag{3}$$

where f_{min} is the bottom level of the step function, ω_* and ω_c are the fastness parameter and its critical value for the propeller transition, and δ is the value of the smoothness. So, the δ parameter is related to the thickness of the inner layer of the accretion disk while f_{min} is linked with the extra luminosity sources other than accretion such as NS cooling in the quiescent level. Since Equation (2) represents the slow decay and Equation (3) is a smoothed step function, multiplication of these two equations can represent the whole decay. Before the knee, step function equals to 1 and only Equation (2) is valid while after the knee L_X goes to quiescent level smoothly. In this study, we applied the technique to the MAXI
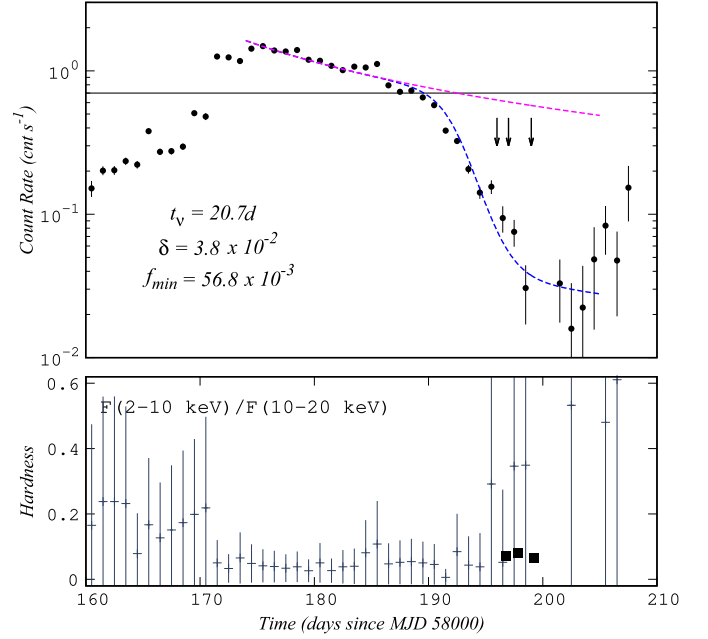

Fig. 3. *Upper panel:* The MAXI light curve of the 2018 outburst of Aql X-1 with the best fit to the model. The pink and the blue curves represent the best fit of Equation (2) to the slow decay stage and $L(t)$ to the whole of the light curve, respectively. The vertical dashed line shows the critical count rate level of the source while propeller transition. The upside-down arrows show the observation times of Insight-HXMT. *Bottom panel*: The hardness evolution along the 2018 outburst obtained from the ratio of the MAXI count rates in the energy ranges of $2.0 - 10.0$ keV and $10.0 - 20.0$ keV. The hardness values obtained from Insight-HXMT data are shown with black filled squares.

light curve of the 2018 outburst of Aql X-1 and obtained the free parameters in the model (Fig. 3). We estimated t_ν of 20.7±1.3 d, δ of $(3.8±1.1)×10^{-2}$ and f_{min} of $(56.6±13.0)×10^{-3}$. The estimated value of δ is consistent with the results of previous outbursts presented by Güngör et al. (2017b). The method allows us to estimate the fastness parameter for a given time using the relation below;

$$\omega_*(t) = \left[\frac{L(t)}{L_c}\right]^{-3/7} \tag{4}$$

where L_c is the critical luminosity at the time of the transition from the accretion stage to the propeller stage (see Güngör et al., 2017b for derivation). The calculated fastness parameters for the times of Insight-HXMT observations are given in Table 1. The given fastness parameters show that the angular velocity of the star is larger than the Keplerian angular velocity in the inner radius of the disk and the material repelled by the centrifugal barrier from the inner layers of the disk to larger radii.

3.3. Spectral output of Insight-HXMT

The first model (model I) is the combination of a blackbody and a power law. We assume that the blackbody represents the thermal radiation from the source and the power law component represents the non-thermal radiation (if any). While, this model gives relatively good reduced chi-square ($\chi^2/d.o.f.$) values (~ 0.87), the blackbody temperatures are very high and evolve to higher values for lower flux levels while the photon indexes are around ~ 2.5 which match with previous results of LMXBs (e.g. Remillard and McClintock, 2006; Seifina et al., 2015) This situation shows that the model must be modified since the blackbody temperatures can not be explained via physical processes even if the data is quite good modelled.
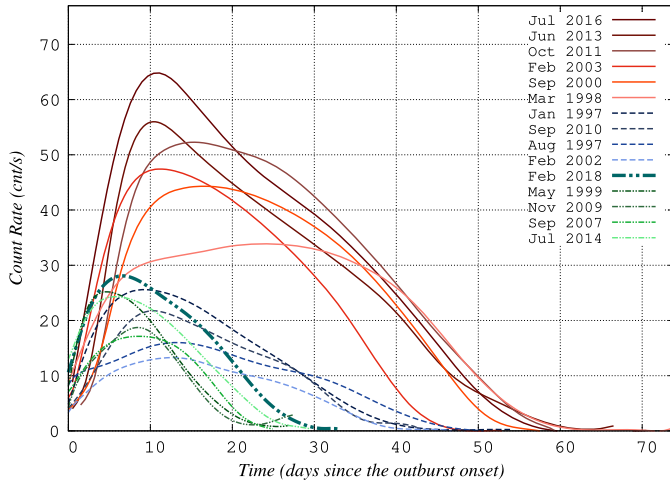
Fig. 4. The light curves of the FRED type outbursts of Aql X-1 calibrated to the beginnings. The light curves are smoothed for easy visualisation. This graph is the revised version of the one presented by Güngör et al. (2017a) by adding the 2018 outburst. The labels are sorted descendingly according to the peak count rate of each outburst. The long-high, the medium-low and the short-low outbursts are shown with different tones of red, blue and green, respectively.

In model II, we implemented a combination of models of blackbody, for the radiation from NS itself and disk blackbody for the contribution of the inner layers of the accretion disk. The temperatures of the blackbody components are also quite high as seen in model I, although the model represents the data well with the $\chi^2/d.o.f.$ of ~ 0.90. The normalization of the disk blackbody model is defined as $(R_{in}/D_{10})^2 \cos\theta$, where R_{in} is the inner disk radius in km, D_{10} is the distance in the unit of 10 kpc and θ is the angle of the disk. The normalization value for the observation of ObsID P011466801001 is 40 which gives $R_{in} = 2.81$ km/$\sqrt{\cos\theta}$ by taking the source distance as 4.5 kpc (Galloway et al., 2008). This value can only give a reasonable value for angles really close to $90°$ (edge on view). Given the fact that this model and the previous one give an unsatisfactory description, we need to add an extra model to take into account comptonization which is expected for LMXBs in low accretion regime.

We checked the effect of the up-scattered photons from the Compton cloud by modelling the spectra using the combination of blackbody and comptonization (model III). This model can also represent the spectra statistically good with $\chi^2/d.o.f.$ of ~ 0.90. The blackbody temperature throughout this model evolves from 0.37 keV to 0.69 keV. These temperatures are lower than the ones obtained from model I and II.

We, then, added the comptonization model to diskbb component (model IV) in which the seed photon temperature of the comptonization model is now linked to the temperature of the inner radius of the disk in diskbb component. The output temperatures of model IV increase in time along three data sets. This is not an expected phenomenon since the inner radius of the disk shrinks back along time at the decay stage of an outburst. The normalization of the diskbb component of the first observation set is ~ 500 which results the inner radius of the disk is $R_{in} = 10.06$ km for face-on viewing angle ($\theta = 0$) for the source distance of 4.5 kpc.

We, lastly, implemented a model which is a combination of a blackbody, a disk blackbody and a comptonization (model V) with the seed photon temperature linked to the blackbody temperature assuming that the up-scattered photons are coming from the NS poles. Similar to the other models the spectra are well fitted with an average $\chi^2/d.o.f.$ of ~ 0.88. On the other hand, we do not see the high blackbody temperatures seen in model I and the normalization of the disk blackbody component is similar to the one obtained from model V which gives a reasonable in-

ner radius of the disk. The F statistic value and its probability of adding the comptonization component are 50.33 and 1.79×10^{-21}, respectively. Low probability and large F−test value shows that adding the third component provides a significant improvement. Ultimately, the most reliable model overall these 5 models is the model V with both its physical interpretation and the acceptable model parameters.

In order to compare spectral output of our analysis, we first found the data with similar fastness parameters in the literature. The fastness parameters of RXTE data with the ObsId of 50049-03-04-00, 96440-01-09-05 and 96440-01-09-12 are 1.06, 1.06 and 1.07, respectively (Güngör et al., 2017b). These three observations were acquired while the source was transiting from the soft-high state to the hard-low state, while the first belongs to the 2000 outburst and the rest belongs to the 2011 outburst. Güngör et al. (2017b) mentioned that the temperature values without comptonization model are too high to be explained via physical processes even if the model may fit the spectrum mathematically well with reasonable $\chi^2/d.o.f.$ values. We see the same situation in our analysis. This strengthens the method created by Güngör et al. (2017b), in which the method can be also used to compare the data in different luminosity levels and the data obtained by different space missions since it is based mainly on using unitless parameters (ω_* and $f \equiv \dot{M}_*/\dot{M}$). Parameters listed in Table 1 show that adding comptonization corrects the high temperatures in model I and model II. This implies that the electron cloud is effective in low accretion rates.

4. Conclusions

We present the output of the spectral analysis of three Aql X-1 observations obtained by Insight-HXMT. We model the spectra in the energy range of $2.0 - 20.0$ keV combining the data from the LE and the ME detectors with a set of models. We compared our results to the ones obtained by RXTE data with similar fastness parameters. Differently from RXTE, Insight-HXMT is able to cover a broader energy range combining LE and ME detectors including energies below 3.0 keV and with its better CCD type energy resolution. We show that the temperatures of the blackbody components are very high to be resulted from physical processes for model I and model II, which demonstrates that these models do not well work in low luminosity/accretion regimes. A comptonization component to take into account the inverse Compton process of up-scattered photons, takes the high blackbody temperatures to reasonable values. This indicates the existence of electron cloud between the inner disk and NS in the low accretion regime.

We study the 2018 FRED type outburst. We show that the 2018 outburst is a member of S-type according to the classification presented by Asai et al. (2012) and belongs to the short-low class according to the classification of Güngör et al. (2014). Applying the technique presented by Güngör et al. (2017b), we show that the Insight-HXMT observations are just after the transition from the accretion stage to the propeller stage. The hardness parameters obtained from MAXI data is unstable at the time of Insight-HXMT observations. But on the other hand, the ones throughout our Insight-HXMT analysis are consistent with the previous trend of MAXI, indicating that the system is still in the high-soft regime or in the transition from high-soft state to low-hard state.

References

Arnaud, K.A., 1996. In: Jacoby, G.H., Barnes, J. (Eds.), Astronomical Data Analysis Software and Systems V. In: Astronomical Society of the Pacific Conference Series, vol. 101, p. 17.

Asai, K., Matsuoka, M., Mihara, T., et al., 2012. Publ. Astron. Soc. Jpn. 64, 128.

Asai, K., Matsuoka, M., Mihara, T., et al., 2013. Astrophys. J. 773, 117.

Bhattacharya, D., van den Heuvel, E.P.J., 1991. Phys. Rep. 203, 1.

Campana, S., Coti Zelati, F., D'Avanzo, P., 2013. Mon. Not. R. Astron. Soc. 432, 1695.

Campana, S., Stella, L., Mereghetti, S., et al., 1998. Astrophys. J. Lett. 499, L65.

Cannizzo, J.K., Lee, H.M., Goodman, J., 1990. Astrophys. J. 351, 38.

Casella, P., Altamirano, D., Patruno, A., Wijnands, R., van der Klis, M., 2008. Astrophys. J. Lett. 674, L41.

Chen, Y.P., Zhang, S., Zhang, S.N., et al., 2019. J. High Energy Astrophys. 24, 23.

Ekşi, K.Y., Kutlu, E., 2011. In: Göğüş, E., Belloni, T., Ertan, Ü. (Eds.), American Institute of Physics Conference Series, vol. 1379, pp. 156–159.

Frank, J., King, A., Raine, D.J., 2002. Accretion Power in Astrophysics, third edition.

Galloway, D.K., Muno, M.P., Hartman, J.M., Psaltis, D., Chakrabarty, D., 2008. Astrophys. J. Suppl. Ser. 179, 360.

Gilfanov, M., Revnivtsev, M., Sunyaev, R., Churazov, E., 1998. Astron. Astrophys. 338, L83.

Göğüş, E., Alpar, M.A., Gilfanov, M., 2007. Astrophys. J. 659, 580.

Güngör, C., Ekşi, K.Y., Göğüş, E., 2017a. New Astron. 56, 1.

Güngör, C., Ekşi, K.Y., Göğüş, E., Güver, T., 2017b. Astrophys. J. 848, 13.

Güngör, C., Güver, T., Ekşi, K.Y., 2014. Mon. Not. R. Astron. Soc. 439, 2717.

Ibragimov, A., Poutanen, J., 2009. Mon. Not. R. Astron. Soc. 400, 492.

Illarionov, A.F., Sunyaev, R.A., 1975. Astron. Astrophys. 39, 185.

Jonker, P.G., Nelemans, G., 2004. Mon. Not. R. Astron. Soc. 354, 355.

Koyama, K., Inoue, H., Makishima, K., et al., 1981. Astrophys. J. Lett. 247, L27.

Lasota, J.-P., 2001. New Astron. Rev. 45, 449.

Li, T.-P., 2007. Nucl. Phys. B, Proc. Suppl. 166, 131.

Lochner, J.C., Remillard, R.A., 1995. In: American Astronomical Society Meeting Abstracts, vol. 187. Abstract 91.05.

Maccarone, T.J., Coppi, P.S., 2003. Astron. Astrophys. 399, 1151.

Maitra, D., Bailyn, C.D., 2008. Astrophys. J. 688, 537.

Mata Sánchez, D., Muñoz-Darias, T., Casares, J., Jiménez-Ibarra, F., 2017. Mon. Not. R. Astron. Soc. 464, L41.

Matsuoka, M., Kawasaki, K., Ueno, S., et al., 2009. Publ. Astron. Soc. Jpn. 61, 999.

Ootes, L.S., Wijnands, R., Page, D., Degenaar, N., 2018. Mon. Not. R. Astron. Soc. 477, 2900.

Pringle, J.E., Rees, M.J., 1972. Astron. Astrophys. 21, 1.

Remillard, R.A., McClintock, J.E., 2006. Annu. Rev. Astron. Astrophys. 44, 49.

Romanova, M.M., Ustyugova, G.V., Koldoba, A.V., Lovelace, R.V.E., 2004. Astrophys. J. Lett. 616, L151.

Seifina, E., Titarchuk, L., Shrader, C., Shaposhnikov, N., 2015. Astrophys. J. 808, 142.

Spiridonova, O.I., Moskvitin, A.S., Vlasyuk, V.V., 2018. The Astronomer's Telegram, 11382.

Tauris, T.M., van den Heuvel, E.P.J., 2006. Formation and Evolution of Compact Stellar X-Ray Sources, pp. 623–665.

Titarchuk, L., Lyubarskij, Y., 1995. Astrophys. J. 450, 876.

Verbunt, F., Belloni, T., Johnston, H.M., van der Klis, M., Lewin, W.H.G., 1994. Astron. Astrophys. 285, 903.

Verner, D.A., Ferland, G.J., Korista, K.T., Yakovlev, D.G., 1996. Astrophys. J. 465, 487.

Zhang, S., Lu, F.J., Zhang, S.N., Li, T.P., 2014. In: Space Telescopes and Instrumentation 2014: Ultraviolet to Gamma Ray. In: Proc. SPIE, vol. 9144, 914421.

Zhang, S.N., Yu, W., Zhang, W., 1998. Astrophys. J. Lett. 494, L71.